Oxygen nonstoichiometry and dielectric evolution of $BaTiO_3$. Part II—insulation resistance degradation under applied dc bias

G. Y. Yang, G. D. Lian,[a] E. C. Dickey, and C. A. Randall
Department of Materials Science and Engineering, Center for Dielectric Studies, and The Materials Research Institute, Pennsylvania State University, University Park, Pennsylvania 16802

D. E. Barber, P. Pinceloup, M. A. Henderson, R. A. Hill, J. J. Beeson, and D. J. Skamser
KEMET Electronics Corporation, 201 Fairview Street Extension, Fountain Inn, South Carolina 29644

(Received 25 May 2004; accepted 1 September 2004)

The microchemical and microstructural origins of insulation-resistance degradation in $BaTiO_3$-based capacitors are studied by complementary impedance spectroscopy and analytical transmission electron microscopy. The degradation under dc-field bias involves electromigration and accumulation of oxygen vacancies at interfaces. The nonstoichiometric $BaTiO_{3-\delta}$ becomes locally more conducting through increased oxygen vacancy concentration and Ti ion reduction. The symmetry across the dielectric layer and locally across each grain is broken during the degradation process. Locally, the nonstoichiometry becomes so severe that metastable lattice structures are formed. The degradation in insulation resistance at the grain boundaries and electrode interfaces is associated with the double Schottky-barrier potential lowering and narrowing. This may correlate with an effective decrease in net acceptor charge density at the grain boundaries. © *2004 American Institute of Physics*. [DOI: 10.1063/1.1809268]

I. INTRODUCTION

A further challenge for the development of high-performance base-metal electrode multilayer ceramic capacitor (BME MLCCs) is to improve the device reliability while increasing volumic efficiency and reducing production cost. The reliability is associated with the time-dependent degradation in insulation resistance of the capacitors, which is characterized by a slow increase in the leakage current under applied direct-current (dc) field stress. Since the net insulation resistance of the MLCC has contributions from the $BaTiO_3$ dielectric layers, $BaTiO_3$ grain boundaries and Ni-$BaTiO_3$ internal electrode interfaces, the degradation in total insulation resistance of the capacitors may be controlled by the degradation of any of or all three microstructural components.[1]

$BaTiO_3$-based MLCCs with Ni internal electrodes are cofired in a reducing atmosphere to avoid oxidation of the electrodes. Despite the reoxidation process, there are still a large number of oxygen vacancies that are accommodated in the $BaTiO_3$ active layers. Long-term failure of BME MLCCs is thought to be dominated by electromigration of oxygen vacancies through the grain boundaries in the dielectric layers.[1–6] Investigation of the degradation phenomenon for air-fired $SrTiO_3$ (*p*-type) and acceptor doped single crystal $SrTiO_3$ and polycrystal dielectric $BaTiO_3$ has been carried out by a number of authors.[1,7–14] It is believed that the degradation in insulation resistance is initiated by the oxygen vacancy electromigration toward the cathode with respect to time, field, and temperature. Dopants and defects have been found to be segregated at the grain boundaries during the sintering process and results in the formation of space charge layers at the grain boundaries. The grain boundary acts as an electrical barrier against the oxygen vacancy electromigration, and thus retards the degradation process.[1,8,15,16] These regions are also depleted of electron carriers and are therefore more resistive. However, with the decrease in dielectric layer thickness within the capacitor, the role of each grain boundary must be optimized as there are fewer grain boundaries between the anodes and cathodes to limit the electronic and ionic transport and maximize total dielectric permittivity. In addition, the internal electrode interface is also a key part of the design as it can control electron injection at the cathode.[17] The insulation resistance of the electrode interface originates from the Schottky contact between the Ni internal electrode and *n*-type $BaTiO_3$. In a study on electrical degradation of Ho-Mg codoped Ni-$BaTiO_3$ MLCC using impedance spectroscopy,[1] it has been suggested that oxygen vacancies are blocked by electrode interfaces. Oxygen vacancies move towards the cathodes under a dc electrical field, resulting in a high concentration of oxygen vacancies near the cathodes.

In this work, impedance spectroscopy (IS) and analytical electron microscopy (AEM) have been used to investigate the local degradation behavior in insulation resistance of commercial Ni-$BaTiO_3$ MLCCs. The correlation between the electrical performance and microstructure, microchemistry, and electronic structure of $BaTiO_3$, $BaTiO_3$ grain boundaries, and Ni-$BaTiO_3$ electrode interfaces are all discussed.

II. EXPERIMENTAL PROCEDURES

The as-produced Ni-$BaTiO_3$ BME MLCCs are fabricated by cofiring $BaTiO_3$ dielectric layers with Ni internal electrodes at ~1300 °C in a P_{O_2} of $\sim 10^{-10}$ atm. Followed

[a]Present address: Process Characterization Laboratory, ATDF Inc., Montopolis Drive, Austin, TX 78741.

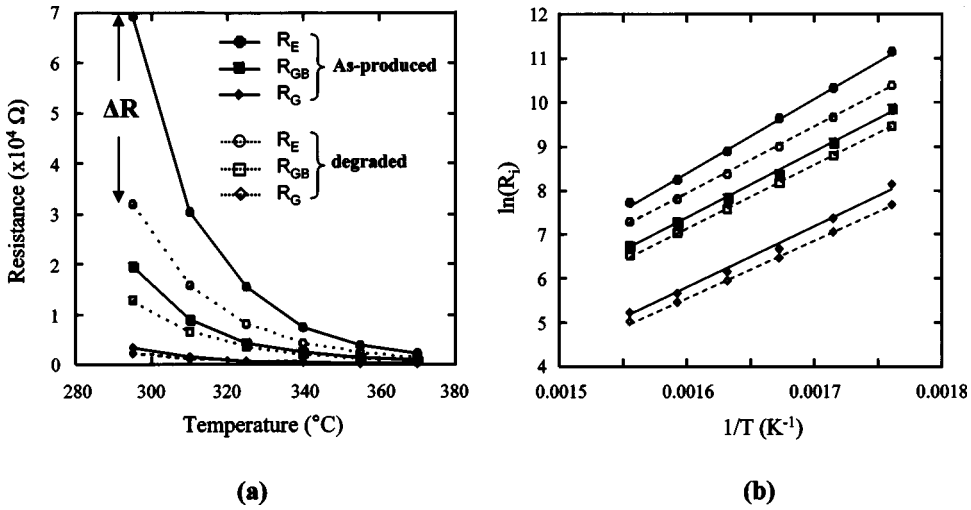

FIG. 1. Resistance changes as a function of capacitor state and temperature. Solid symbols represent the data obtained from the as-produced capacitors and open symbols the data from degraded capacitors over the temperature range of 295–370 °C. (a) variation of insulation resistances (R_i) versus temperature T showing the relationship of $R_E > R_{GB} > R_G$, and (b) the natural log of the resistance versus inverse absolute temperature.

by an annealing at ~800 °C in a P_{O_2} of $\sim 10^{-8}$ atm. The dimension of the capacitor is $3.5 \times 2.5 \times 1.15$ mm^3 with Ni electrode thickness of 2 μm and active layer thickness about 12 μm. The devices have a capacitance of 2.2 μF. Resistance degradation of the MLCCs is characterized by a slow decrease in insulation resistance under simultaneous temperature and dc field stress. The as-produced capacitors are degraded with a highly accelerated life test (HALT). The HALT tests are performed at 140 °C under 400 V dc field until the insulation resistance of the MLCC becomes lower than 90% of its initial value.

The impedance of the as-produced and degraded MLCCs are measured using a *Solartron* SI1287 electrochemical interface and 1255B frequency response analyzer with V_{rms} at 100 mV under N_2 atmospheres to avoid oxidation of the end copper terminations of the MLCCs. Experimental data are fitted with theoretical models based on proposed 3RC equivalent circuits using the electrochemical impedance software *Z*-view for Windows (*Scribner Associates*).[18,19] Errors are calculated from a least-squares approach of the fitted data.

AEM is used in a complementary fashion to correlate the insulation resistance degradation of the Ni-$BaTiO_3$ capacitors to the microstructure/microchemistry changes in the capacitors. Cross-sectional TEM samples of the Ni-$BaTiO_3$ MLCCs are prepared following the same procedures described in Part I.[18] Microstructural and microchemical studies of the BME MLCCs are performed using a JEOL transmission electron microscope equipped with a field emission gun (JEOL 2010F) operating at 200 kV. Energy dispersive spectroscopy (EDS) is carried out with the Emispec system in scanning transmission electron microscopy (STEM) mode. Electron energy-loss spectroscopy (EELS) is performed with a Gatan Enfina parallel electron energy-loss spectrometer attached to the JEOL 2010F microscope. The energy resolution at the zero-loss peaks is about 1.1 eV (full width at half maximum). EELS are recorded in TEM-diffraction mode with a collection angle of 14 mrad, and analyzed with Gatan DigitalMicrograph software.

III. RESULTS AND DISCUSSIONS

A. Impedance spectroscopy analysis

The degradation in insulation resistance of each structural component, upon HALT tests, has been monitored with (IS). Figure 1(a) shows the changes of insulation resistance of Ni electrode interfaces, $BaTiO_3$ grain boundaries, and bulk $BaTiO_3$ grains as a function of temperature from 295 to 370 °C. The insulation resistances associated with different circuit elements are identified from the impedance spectra by fitting the experimental data with 3RC equivalent circuit as explained in Part I.[18] The solid symbols and open symbols represent the resistance values of as-produced and degraded capacitors, respectively. The resistances decrease with increasing measurement temperature. Decreases in insulation resistances are simultaneously observed in the degraded capacitors across all three RC elements. The relationship of $R_E > R_{GB} > R_G$ (where E, GB, and G denote electrode, grain boundary, and dielectric grain) indicates that the Schottky barriers at grain boundaries and electrode interfaces play an important role in total insulation resistance of the Ni-$BaTiO_3$ MLCCs.

Activation energies for each circuit element are calculated from the slopes of $\ln(R_i)$ versus $1/T$ [Fig. 1(b)] since the resistances vary as a function of temperature, following

$$R_i = R_0 \exp(E_{A,i}/kT), \tag{1}$$

where R_0 is a constant, $E_{A,i}$ is the activation energy for conduction for the ith circuit element, k the Boltzmann constant, and T absolute temperature. The values of each activation energy $E_{A,i}$ are listed in Table I. The values of $E_{A,i}$ of the as-produced capacitor are in good agreement with earlier studies.[19] The activation energies of each element in the degraded capacitors are significantly lowered, implying that each element in the degraded capacitors becomes more conducting on degradation under the simultaneous temperature and dc electrical field stress.

TABLE I. Activation energies of electrode interfaces, grain boundaries, and dielectrics in the as-produced and degraded MLCCs.

	E_A (eV)		
Capacitors	Electrode interfaces	Grain boundaries	Grains
As-produced	1.45±0.02	1.30±0.02	1.21±0.03
Degraded	1.29±0.01	1.23±0.01	1.11±0.02

B. Analytical electron microscopy studies

AEM is used to correlate microstructural and microchemical changes of the degradation in insulation resistance of Ni-$BaTiO_3$ MLCCs. The evolution of microstructure is discussed for all three circuit elements before and after the degradation process.

1. $BaTiO_3$ *dielectric layers*

Figures 2(a) and 2(b) show typical bright-field TEM micrographs of $BaTiO_3$ grains in the as-produced and degraded capacitors. There exist a few structural defects in the as-produced capacitor [Fig. 2(a)]. However, Fig. 2(b) shows that the structural defects are frequently observed in the degraded capacitors. These defects are identified as linear defects that are associated with aggregation of oxygen vacancies. The distribution of the defects is inhomogeneous throughout the dielectric layers of the degraded capacitors. The dislocation loops that are noted by the arrows in Fig. 2(b) are considered to be associated with reduction and a clustering of vacancies.[20,21] Local EELS analysis of the loop dislocations indicates local oxygen deficiency and Ti reduction.[22] The structural defects can be suppressed through reoxidation and we do not observe many of these types of defects in the as-produced capacitors. Upon degradation under electrical field stress, local accommodation and clustering of oxygen vacancies occurs and induces microstructural defects. In addition to dislocation loops in the degraded capacitors, we recently discovered a modulated lattice structure in the $BaTiO_{3-\delta}$.[23] The modulated structure is observed when the $BaTiO_3$ grain is orientated to have its $\langle 110 \rangle$ zone axis parallel to the incident electron beam.[23,24] The modulated structure shown in Fig. 2(c) is associated with the clustering of oxygen vacancies in the framework of the $BaTiO_3$ lattice under either strong reduction conditions or electromigration of the vacancies towards the cathodes.[18,23] The satellites surrounding the matrix electron diffraction reflections (see the inset) are correlated to an incommensurate structural modulations created from oxygen-vacancy and Ti^{3+}-Ti^{4+} ordering on the $\{111\}$ planes.[24]

2. $BaTiO_3$ *grain boundaries*

IS results in Fig. 1 show that $R_{GB} > R_G$ in both as-produced and degraded capacitors, indicating that $BaTiO_3$ grain boundaries act as resistive barriers across the dielectric layer. The barriers originate from *n*-type semiconducting $BaTiO_3$ band-bending at the grain boundaries to form back-to-back Schottky barriers. The *n*-type grains result from the high concentration of oxygen vacancies from the low P_{O_2} firings of the base-metal dielectrics. The acceptors at the grain boundary enhance the potential barrier which in turn enhances high grain boundary resistivity. In this work, the dopant distribution is studied using EDS to confirm uniform distribution of key dopants used to engineer the dielectric temperature dependence and lifetime behavior of X7R-type Ni-$BaTiO_3$ MLCCs.[2–4,25] Figure 3(a) shows a typical dark-field STEM image of a $BaTiO_3$ grain boundary of the as-produced MLCC. The grain boundary is tilted to be parallel to the incident electron beam and the adjacent grains are orientated away from strong diffraction conditions to avoid electron channeling effects. The spectra are taken in STEM mode from an area 60×12 nm^2 crossing the grain boundary and two regions that are about 50 nm away from the grain boundary under the identical experimental conditions. The EDS data obtained from the grain interiors are used as an internal standard to determine the dopant segregation at the grain boundaries. Figure 3(b) shows a set of EDS spectra obtained from the $BaTiO_3$ grain boundary and grain interiors ($A1$, $A2$ regions) of the as-produced capacitor. Note that the Ti $K\alpha$ and Ba $L\alpha$ peaks overlap and are difficult to distinguish. Cu peaks arise from the copper TEM grid. Si is attributed to the sintering-aid glass additives. Peaks associated with the Ca, Mn, and Y dopants are evident in the spectrum obtained from the grain boundary. The Mn cations are typical acceptor dopants and occupy Ti sites in the $BaTiO_3$ lattice. If Ca occupies the Ti sites, it will behave as an acceptor. The Y^{3+} can be soluble on both Ba and Ti sites and is termed and amphoteric cation.[26,27] This dopant acts as a donor when substituted into the Ba sites or as an acceptor when on the Ti sites. Taking the amphoteric dopant Y_2O_3 as an example, the inset shows significant Y dopant segregation at the grain boundary. The dopant segregation plays an important role in the formation of back-to-back double Schottky barriers at the

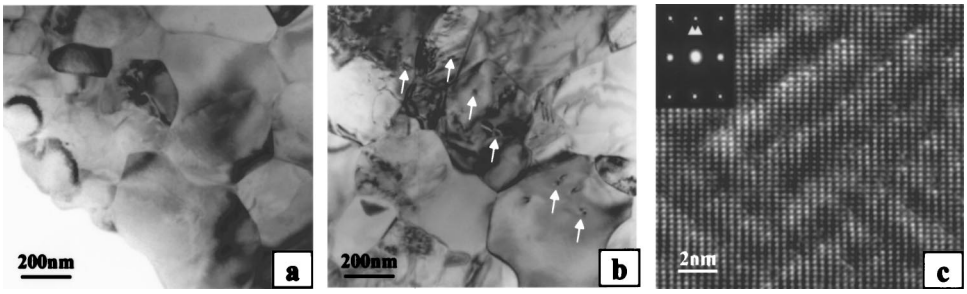

FIG. 2. (a) Bright-field micrograph showing the defect-free $BaTiO_3$ of the as-produced capacitor. Bright-field (b) and high-resolution (c) images indicating the high density of linear defects and modulated defects in the $BaTiO_3$ of the degraded capacitors.

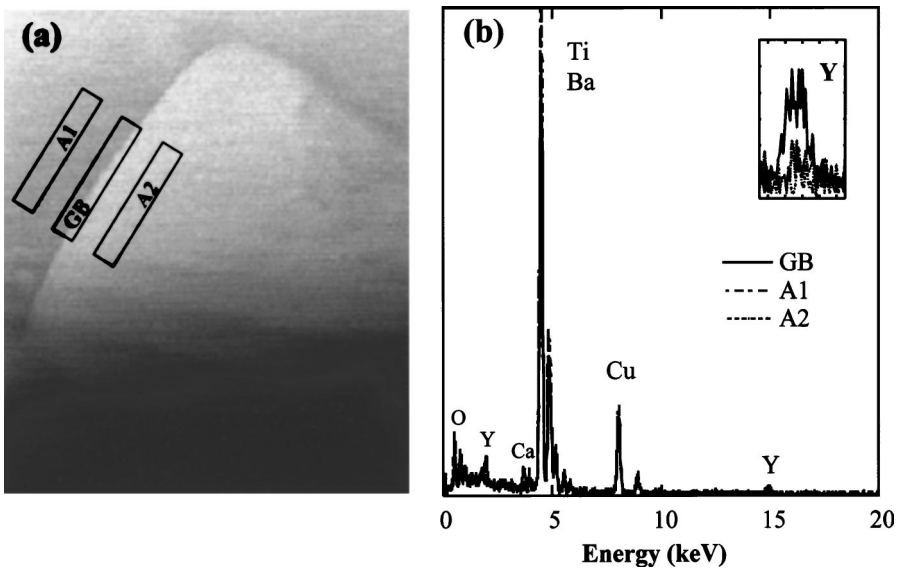

FIG. 3. (a) Typical dark-field image of a $BaTiO_3$ grain boundary showing the areas used for EDS analysis, and (b) EDS spectra obtained at grain boundary and grain interiors. Dopant segregation to the grain boundary is observed.

grain boundary, which aids in the resistance enhancement of $R_{GB} > R_G$. The importance of this grain boundary barrier effect has been demonstrated with an excellent set of systematic dopants studies with Ho_2O_3-MgO doped $BaTiO_3$ by Chazono *et al.*[28]

Dopant segregation to grain boundaries is also observed in the degraded capacitors and no obvious changes in the dopant segregations are evident. However, it is difficult to determine quantitatively the dopant concentration at the grain boundary due to the superposition of the Ti $K\alpha$ and Ba $L\alpha$ peaks.

Figure 4(a) shows a bright-field image of $BaTiO_3$ and grain boundaries in an as-produced capacitor. The image is taken with the incident electron beam parallel to the $[10\bar{1}]$ zone axis of grain *A*. The $BaTiO_3$ grains are free of linear defects and structural modulations. All diffraction spots in the insert are indexed as the basic reflections of the pseudocubic $BaTiO_3$ structure. Shown in Fig. 4(b) is an enlarged part of the grain boundary between grains *A* and *B*. The grain boundary is sharp at the atomic level and free of any additional phases, such as precipitates or amorphous phases.

Figure 5(a) shows a bright-field image of $BaTiO_3$ and grain boundaries in the degraded capacitors and Fig. 5(b) is a high-resolution image of the grain boundary between adjacent grains *A* and *B*. The images are obtained with the incident electron beam parallel to the $[10\bar{1}]$ zone axis of grain *A*. In addition to the basic reflections of the pseudocubic $BaTiO_3$ lattice, satellite reflections are apparent in the inserted diffraction pattern, consistent with the nonstoichiometric structural modulations in the $BaTiO_3$. The wavylike image contrast in grain *A* originates from the structural modulation of nonstoichiometry in the oxygen sublattice framework of the $BaTiO_3$. However, the image contrast associated with the modulated structure is discontinuous around the grain boundaries. The defect contrast becomes faint near the grain boundary regions as noted by the dashed lines, indirectly implying that oxygen content in this grain boundary region is higher than those grain interiors and other parts of the grain boundary regions. The thickness of this nonmodulated region at the grain boundary is approximately

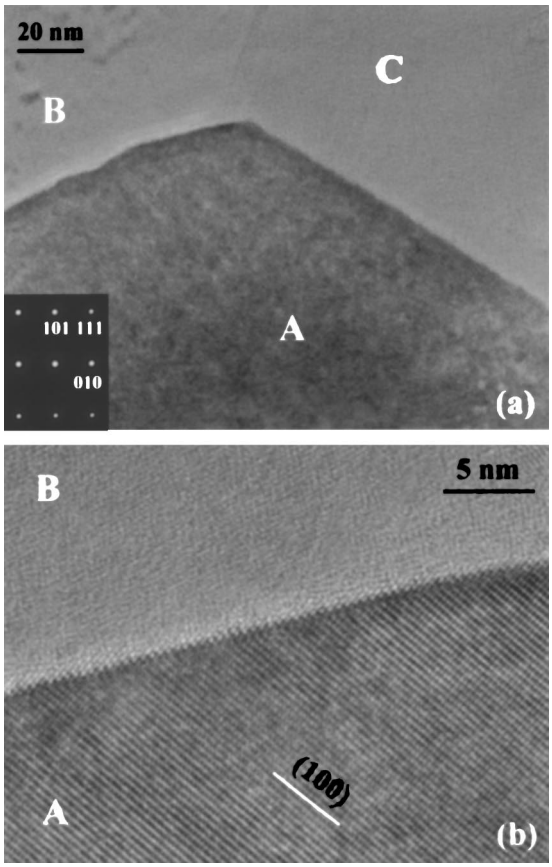

FIG. 4. (a) Bright-field TEM image and (b) high-resolution TEM image showing the grain boundaries free of structural defects and precipitates in the as-produced MLCC.

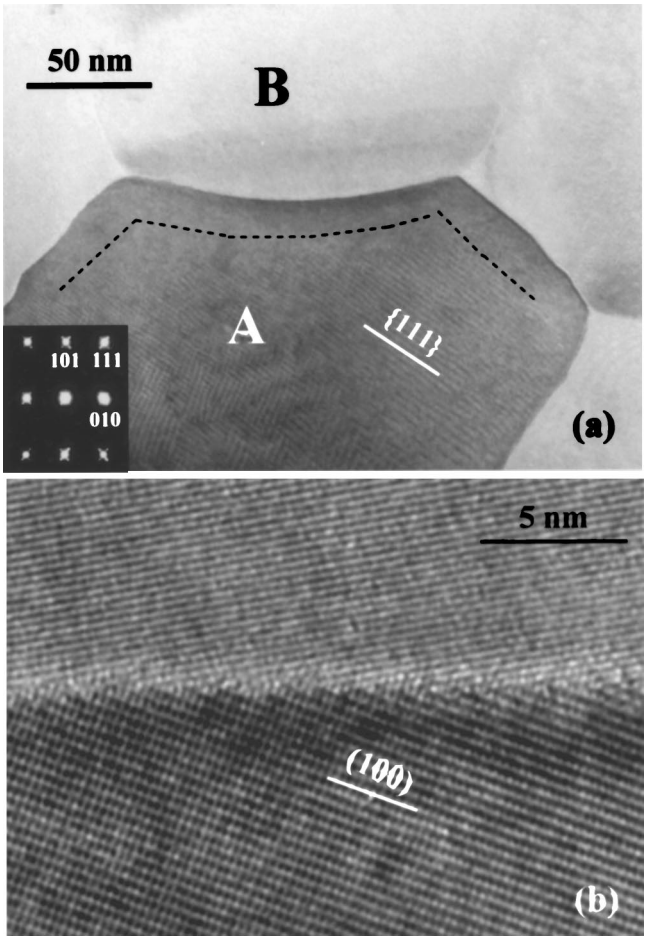

FIG. 5. (a) Bright-field TEM image and (b) high-resolution TEM image showing the grain boundaries free of any precipitates in the degraded MLCC. The modulated defect appears discontinuously around the grain boundary and the thickness of the nonmodulated region at the grain boundary is about 25 nm.

25 nm. The high-resolution TEM image in Fig. 5(b) indicates that the $BaTiO_3$ grain boundary is atomically abrupt and free of any precipitates.

In a previous paper we have shown that defective $BaTiO_3$ grains may have a mixed microstructure in which regular perovskite structure coexists with the modulated structure in the degraded capacitors.[23] Figures 6(a) and 6(b) show two typical distributions of the modulated phase in the degraded capacitors along a $\langle 110 \rangle$ zone axis. In Fig. 6(a) the modulated structure appears only in the right part of the grain, i.e., an asymmetry of the microstructural distribution is present throughout each individual $BaTiO_3$ grain in the highly degraded regions. Although it is difficult to perform a systematic observation on the distribution of the modulated structure in $BaTiO_3$ grains with respect to electrode polarization, it is reasonable to suggest that the left side and right side of the $BaTiO_3$ grain are toward the anode and cathode in MLCCs, respectively, as indicated by the arrows. In Fig. 6(b), the modulated structure appears discontinuously throughout the grain. The structural modulation occurs only in the regions near grain boundaries and a regular $BaTiO_3$ structure remains in the center of the $BaTiO_3$ grain. Figure 6(c) is an enlarged image of left side part of Fig. 6(b). This part of $BaTiO_3$ grain is free of structural modulations within approximately 30 nm from the grain boundary. On the other hand, the modulation extends to grain boundary at the right side of the grain, as shown in the enlarged image in Fig. 6(d). The modulated structure in the next adjacent grain does not begin until about 40 nm away from the grain boundary. It is known that the modulated structure is formed by clustering of oxygen vacancies in the $BaTiO_3$ grains.[23,24] So under the dc field stress, oxygen vacancies electromigrate from the anode toward the cathode, and the distribution of modulated defect throughout the $BaTiO_3$ grains can be observed as the oxygen vacancy concentration increases. At grain boundaries the barriers to the electromigration result in a pileup of oxygen vacancies in the region toward cathode when the grain boundaries are perpendicular to the applied field. This results in a modification to local transport rates and the redistribution of oxygen vacancies, and forms a local asymmetry in the oxygen microchemistry. It should also be pointed out that the grain boundaries parallel to the applied field often have the modulation up to the grain boundaries and therefore do not significantly limit in ionic conduction of the oxygen vacancies.

The Ti oxidation state and oxygen content in grain boundary regions is investigated using EELS on the capacitors before and after degradation process. Figure 7 shows a set of EELS spectra obtained from grain boundary regions and grain interiors of the as-produced [spectra(a) and (b)] and degraded capacitors [spectra (c) and (d)], respectively. The spectra are calibrated and positioned on the onsets of the O *K* edge (532 eV). The Ti $L_{2,3}$ and O *K* edges are indicated. The Ti L_3 edges of the spectra (a)–(c) are split. The splitting of the Ti $L_{2,3}$ edges is due to spin-orbit coupling and can be attributed to t_{2g} and e_g molecular orbitals, typical for a octahedral coordination of Ti with O.[29,30] The fine structure of O *K* edge fine structure is controlled by the oxygen content and the linear Ti–O bond in the perovskite.[31] Similar shapes of Ti $L_{2,3}$ and O *K* edges for spectra (a) and (b) indicate that Ti-O configurations do not significantly change from grain boundary region to grain interior in the as-produced capacitor. For the degraded capacitor, spectrum (c) is obtained from a grain boundary region where $BaTiO_3$ is free of structural modulation and spectrum (d) from the regions (grain interior or grain boundary) where the modulated defect structure is present, as shown in Figs. 5(a) and 6. Apparent fine structure changes in the Ti $L_{2,3}$ and O *K* edges (*A*, *B*, *C*, and *D* peaks) are observed from spectrum (c) to spectrum (d). In spectrum (d) the splitting of Ti $L_{2,3}$ edges disappears and the intensity of peak *A* under O *K* edge is reduced, indicating a perturbation of the Ti-O octahedral coordination due to the decrease in oxygen content in reduced areas of the degraded capacitor. The calculated nonstoichiometry of the barium titanate in different regions for different capacitor status is listed in Table II, which are determined through integrating the counts under the Ti $L_{2,3}$ and O *K* peaks for the spectra (c)–(d) by following the same approach in a previous paper.[23] The $BaTiO_3$ regions with a large concentration of oxygen vacancies in the grain boundary regions have modulated defects, and those without high concentration of oxygen vacancies lack modulation.

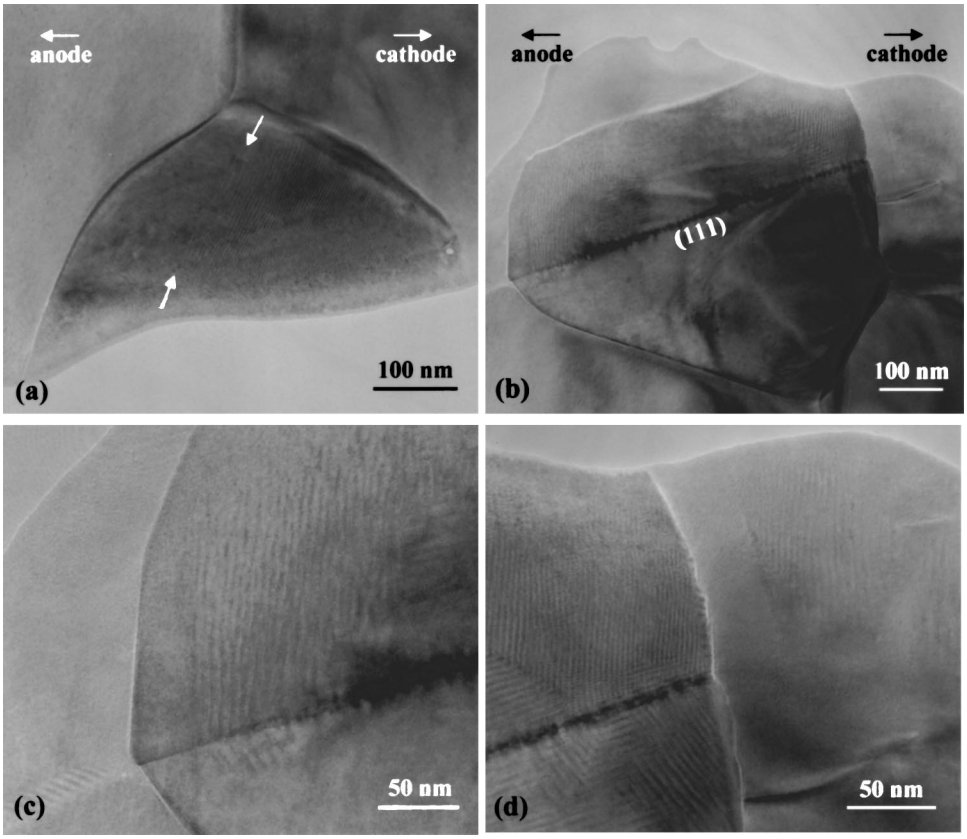

FIG. 6. Bright-field image showing typical distributions of modulated defect throughout individual $BaTiO_3$ grain in the degraded capacitors.

The Ba-O configuration is known to be more stable than that of Ti-O in the $BaTiO_3$ lattice. So the variations in the fine structure of Ti $L_{2,3}$ and O K edges should correlate to the changes in Ti-O configuration. Together, Figs. 6 and 7 provide evidence of the symmetry break in oxygen vacancy distribution across the $BaTiO_3$ grains in the degraded capacitors. With this knowledge of the correlation between microstructure and microchemistry in the grain boundary of the degraded capacitors, we can speculate on the observed changes in the IS data. From the data shown in Fig. 1, we observe the net resistance drops in both grain and grain boundary components in the degraded samples. Also the data listed in Table I indicate the lowering of the activation energies upon degradation. The changes in EEL spectra, modulated microstructure, and electron diffraction pattern indicate a major change in the $BaTiO_3$ structure, in particular with the Ti-O bonding and oxygen vacancy content. We would expect such changes in oxygen content to severely alter the band structure controlling the conduction across the grains, and the grains will be more conductive.

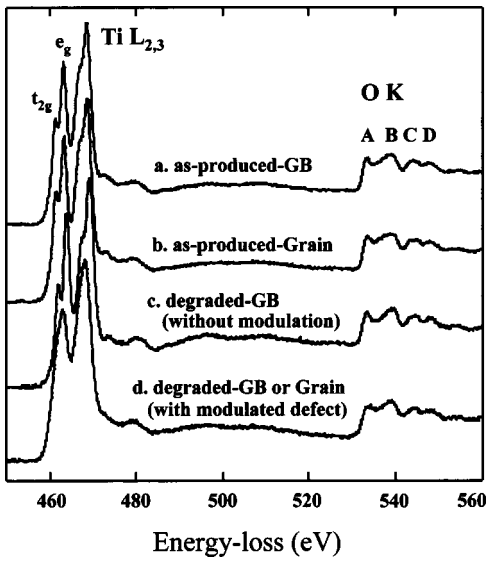

FIG. 7. EELS spectra obtained from the grain boundary region and grain interior of the as-produced and degraded capacitors.

The grain boundary regions start with a homogeneous distribution of oxygen content in the as-produced capacitors. In addition, high performance BME-MLCCs require an enrichment of the amphoteric and acceptor dopants concentration in the grain boundary regions.[2–4] As shown earlier in bulk studies of amphoteric dopants in $BaTiO_3$ oxygen vacancies can be buffered in the site changing of an amphoteric dopant.[26,27] The same reactions are expected to occur at low

TABLE II. Stoichiometry of barium titanate at grain boundaries and grain interiors of the as-produced and degraded MLCCs.

Spectrum	$BaTiO_{3-\delta}$
As-produced GB	$BaTiO_{2.94\pm0.06}$
As-produced grain	$BaTiO_{2.94\pm0.06}$
Degraded GB (modulated defect free)	$BaTiO_{3.00\pm0.06}$
Degraded GB and/or grain (with modulated defect)	$BaTiO_{2.60\pm0.06}$

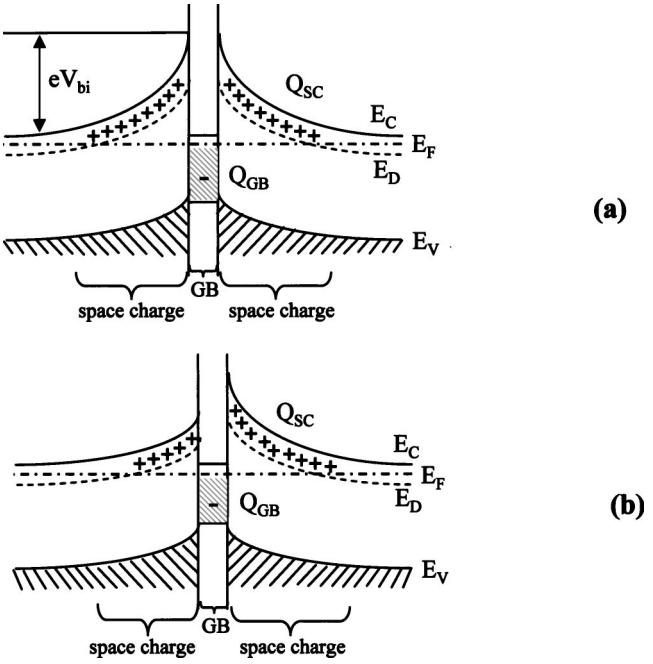

FIG. 8. Schematic presentation of changes in Schottky barrier height eV_{bi} as a function of acceptor charge density at the grain boundaries. (a) The case for the as-produced capacitor and (b) for the degraded capacitor.

temperature in the grain boundary regions. Earlier, we noted that a mass-action relation can control the relative concentrations of amphoteric doping on the *A* and *B* sites, and this is proportional to the oxygen vacancy concentration via

$$[Y_{Ba}^{*}]/[Y_{Ti}'] \propto [V_O^{**}]. \quad (2)$$

Such a reaction reduces the total concentration of acceptor charge in the grain boundaries, and leads to a reduction in the band-bending and accommodates the oxygen vacancy. Eventually, a less negative grain boundary charge is developed and requires a less positive space charge compensation in the space charge layer as $Q_{GB}=-Q_{SC}$.[32] The changes in Schottky barrier heights eV_{bi} as a function of acceptor charge density at the grain boundaries are schematically presented in Fig. 8. In the as-produced capacitor, the Schottky barrier is symmetrical across the grain boundary, as shown in Fig. 8(a). In the degraded capacitor, this symmetry is broken due to oxygen vacancies redistribution and the changes in Y site occupancy. The barrier height is lowered at the side with more Y occupying Ba sites. This is schematically shown in Fig. 8(b). Since the two halves of the grain boundaries are no longer identical, upon degradation, field-drop will be stronger at the grain boundary side with higher barrier height. This results in an effective lowering of the activation energy across the grain boundary in the degraded capacitors (Table I).

3. Electrode interfaces

The microstructure of $BaTiO_3$ grains is systematically examined in the regions near adjacent anode and cathode pairs. The structures of dielectric grains are identical from anode to cathode in the as-produced capacitors. However, as shown in Figs. 9(a) and 9(b), microstructures of $BaTiO_3$ grains are very inhomogeneous in the degraded capacitors with a high density of structural defects locally present near the cathodes. The dislocation loops are marked by the arrows in the image. The density of the defects is low in the dielectric grains next to the anode compared to those near the cathode.

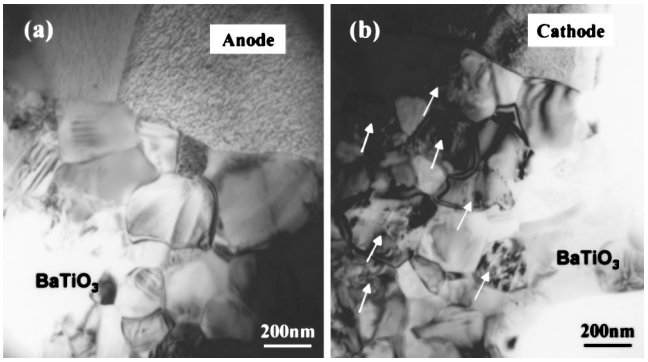

FIG. 9. Bright-field images of the $BaTiO_3$ dielectrics at the anode side (a) and at the cathode side (b). The dislocation loops associated with oxygen vacancies are observed in the $BaTiO_3$ near the cathode.

Coupled with TEM observations represented in Fig. 9, oxidation states of the Ti in $BaTiO_3$ are studied using EELS on more than five anode-cathode pairs. Figure 10 shows typical EEL spectra obtained from the centers of the $BaTiO_3$ grains that are directly contacted with the anode [spectrum (a)] and cathode [spectrum (b)] of the degraded MLCC, respectively. Apparent changes in the fine structures of Ti $L_{2,3}$ edges and O *K* edge are observed from spectra (a) to (b). The fine structures of Ti $L_{2,3}$ and O *K* edges in spectrum a are similar to those in the spectrum obtained from the stoichiometric $BaTiO_3$.[23] In spectrum (b), no apparent sharp splitting of Ti $L_{2,3}$ edges is present, indicating a perturbation in Ti-O octahedral coordination in $BaTiO_3$ at cathode side due to highly oxygen deficiency. Since titanium ions in barium titanate are octahedrally coordinated to oxygen as they are in rutile, the evolution in fine structures of Ti $L_{2,3}$ and O *K* edges from spectra (a) to (b) are similar with those published energy loss near-edge fine structure (ELNES) from Ti^{4+} as it is successively reduced to Ti^{3+} and Ti^{2+}.[33,34]

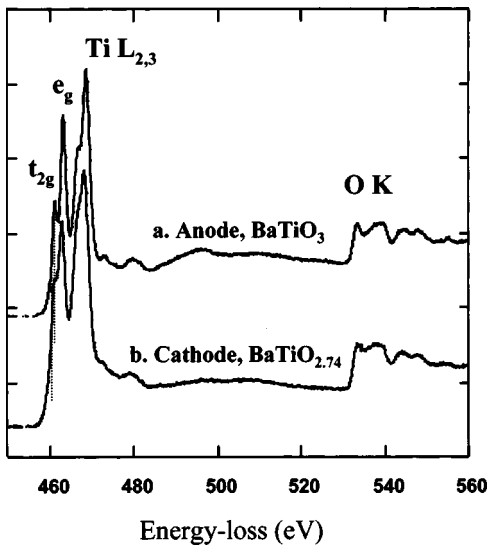

FIG. 10. EEL spectra obtained from the $BaTiO_3$ contacted with the anode (a) and with the cathode (b) of the degraded BME capacitors showing the oxygen deficiency of $BaTiO_3$ at cathode side.

Following the approaches described previously,[23] the stoichiometries of $BaTiO_3$ at anode and cathode sides are calculated. The corresponding formulas of the barium titanate are given in Fig. 10. It is evident that the oxygen vacancies experience an electromigration toward the cathodes in an applied dc electric field due to their positive charge. The electromigration of oxygen vacancies toward the cathode leads to a depletion of oxygen vacancies in the anodic region and an enrichment in the cathodic region. Since the metallic anodes and cathodes block the oxygen transfer, the capacitor is decoupled from the ambient atmosphere, and the total number of oxygen vacancy is conserved in the electrolyte.

Additional evidence for the concentration enhancement of oxygen vacancies in $BaTiO_3$ grains on the cathode side comes from the shift of Ti $L_{2,3}$ edges toward lower energy loss. The shift is quantified by positions of the Ti L_3 onsets (noted by the dashed lines in Fig. 10) after placing the onsets of the O K edges at the same energy loss (532 eV) for spectra (a) and (b). The shift of the Ti L_3 edge onset of about 0.9 eV down in energy is observed from spectrum (a) to spectra (b), indicating a chemical shift from anode to cathode. Since lower oxidation states of titanium cause chemical shifts to lower energy losses,[35–37] this shift down in energy is associated with the reduction of the Ti cations. Further, the shift of the edge onset to lower energy may be associated with a lower band gap in $BaTiO_3$ grains at cathode sides.[38]

It is evident that within the $BaTiO_3$, the Ti cation under sufficient reducing conditions will modify the Ti valence. The electromigration of oxygen vacancies between anode and cathode results in the oxidation of Ti ions at anode side through $Ti^{3+} \rightarrow Ti^{4+} + e'$ and the reduction of Ti ions at cathode side through $Ti^{4+} + e' \rightarrow Ti^{3+}$ and/or $Ti^{3+} + e' \rightarrow Ti^{2+}$, i.e., the oxygen vacancies are compensated by a decrease in the Ti valence at cathode side and/or electron injection are trapped near the cathode region. The Ti cation may have mixed valence states in the dielectrics.[24] The oxygen vacancies pile up at the metal conductor and this increases the effective donor content and reduces the resistance at the electrode interface, driving the non-Ohmic contact toward an Ohmic contact.[39] These types of interfaces are sometimes referred to as accumulation or graded contacts.

The results presented in Part I of this work show that oxygen vacancy concentration is to all intensive purposes homogeneous in the as-produced MLCCs.[18] When applying a dc field to the capacitor, oxygen vacancies electromigrate from the anode to cathode. The redistribution and/or aggregation of oxygen vacancies results in the formation of the modulated defects in the $BaTiO_3$. The grain boundary retards the oxygen vacancy transport, resulting in an asymmetrical distribution of the oxygen content throughout individual $BaTiO_3$ grains. However, the hindrance effect only reduces the transport, and is not 100% effective. The local and macroscopic distribution of oxygen vacancy in the degraded capacitors is schematically presented in Fig. 11. Locally high concentrations of oxygen vacancy near the cathode and at the side of grain boundary toward cathode may lead to the leakage current increase during degradation, eventually the device breakdown occurs at the end of life of the Ni-$BaTiO_3$ MLCCs.

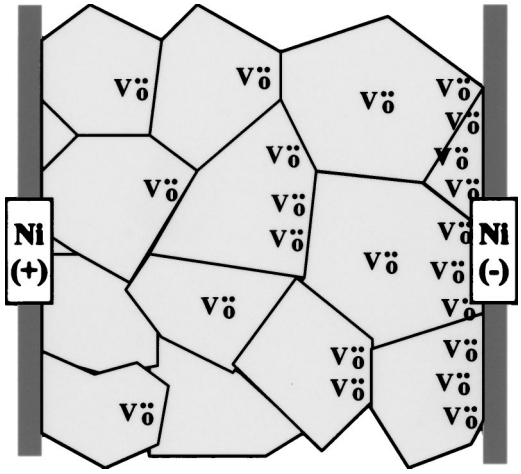

FIG. 11. Schematic presentation of oxygen vacancy concentration in the degraded Ni-$BaTiO_3$ MLCC.

IV. SUMMARY AND CONCLUSIONS

IS offers an electrical means to monitor the changes in resistance and capacitance for the grains, grain boundaries, and electrode-grain interfaces of a multilayer ceramic capacitor during degradation. From earlier studies on reoxidation (Part I), it is inferred that the $BaTiO_3$ is an n-type semiconductor, with the major defects resulting from high concentration of oxygen vacancies created during the thermal processing of the devices. Both in this work and in the earlier studies performed by Chazono and Kishi,[1] it is clear that the electrical performance of the Ni-based X7R MLCCs depends greatly on the higher resistant interface regions of the grain boundaries and electrode interfaces to limit electrical conduction of electrons and also the transport of oxygen vacancies across the dielectric layers.

Combined with analytical and high-resolution transmission electron microscopy we provide more insights into the degradation process. In particular, EELS allows for direct determination of the oxygen content and titanium valence distributions after degradation. There is an increase in the concentration of oxygen vacancy across the dielectric layers towards the cathode, and within each $BaTiO_3$ grain there is a pileup of oxygen vacancy at the cathodic side of the grain due to the blocking effects of the grain boundaries. In contrast, towards the anodic electrode side there is a net decrease in the concentration of oxygen vacancy. Furthermore, there are more linear defects in the $BaTiO_3$ grains towards the cathode side corresponding to oxygen vacancy clustering. However, the most important defects can be imaged by tilting the grains to a $\langle 110 \rangle$ orientation, and then a modulation on $\{111\}$ planes can be observed, along with satellite reflections in the selected-area diffraction patterns. Detailed analysis of this modulation reveals an asymmetric distribution in each grain, and the EELS analysis shows the modulation corresponds to the asymmetric oxygen content distribution in the highly degraded capacitors. This microstructure and its positional asymmetry are consistent with the grain boundary acting as a barrier to the positively charged oxygen vacancies. The EDS analysis of grain boundaries shows there is amphoteric dopant (Y^{3+}) and acceptor dopant enrichment at

the grain boundaries. At this point we know that their segregation is of great importance in BME MLCCs; however, the precise mechanism by which they improve degradation resistance is not directly proven. Further works to determine the precise nature of the segregation distribution in the core and space charge region need to be directly monitored as oxygen vacancies penetrate to the double Schottky potentials.

ACKNOWLEDGMENTS

This work has been supported in part by the NSF-I/UCRC Center for Dielectrics Studies (CDS) and KEMET Electronic Corporation. We also thank CDS members for useful discussions and Materials Research Institute TEM facilities at the Pennsylvania State University, University Park.

[1]H. Chazono and H. Kishi, Jpn. J. Appl. Phys., Part 1 **40**, 5624 (2001).
[2]K. Morita, Y. Mizuno, H. Chazono, and H. Kishi, Jpn. J. Appl. Phys., Part 1 **41**, 6957 (2002).
[3]H. Chazono and H. Kishi, Key Eng. Mater. **248**, 183 (2003).
[4]H. Chazono and H. Kishi, Key Eng. Mater. **216**, 47 (2002).
[5]D. F. K. Hennings, J. Eur. Ceram. Soc. **21**, 1637 (2001).
[6]K. Albertsen, D. Hennings, and O. Steigelmann, J. Electroceram. **2**, 193 (1998).
[7]R. Waser, J. Am. Ceram. Soc. **72**, 2234 (1989).
[8]R. Waser, T. Baiatu, and K. H. Härdtl, J. Am. Ceram. Soc. **73**, 1645 (1990).
[9]R. Waser, T. Baiatu, and K. H. Härdtl, J. Am. Ceram. Soc. **73**, 1654 (1990).
[10]T. Baiatu, R. Waser, and K. H. Härdtl, J. Am. Ceram. Soc. **73**, 1663 (1990).
[11]J. Rödel and G. Tomandl, J. Mater. Sci. **19**, 3515 (1984).
[12]E. Loh, J. Appl. Phys. **53**, 6229 (1982).
[13]W. A. Schulze, L. E. Cross, and W. R. Buessem, J. Am. Ceram. Soc. **63**, 83 (1980).
[14]S. Rodewald, J. Fleig, and J. Maier, J. Am. Ceram. Soc. **83**, 1969 (2000).
[15]M. Vollman and R. Waser, J. Am. Ceram. Soc. **77**, 235 (1994).
[16]H. Kishi, Y. Mizuno, and H. Chazono, Jpn. J. Appl. Phys., Part 1 **42**, 1 (2003).
[17]D. P. Cann and C. A. Randall, J. Appl. Phys. **80**, 1628 (1996).
[18]G. Y. Yang, E. C. Dickey, C. A. Randall, D. E. Barker, P. Pinceloup, M. A. Henderson, R. A. Hill, J. J. Beeson, and D. J. Skamser, J. Appl. Phys. **96**, 7492 (2004).
[19]J. E. Clayton, G. Y. Yang, E. Furman, D. Martin, E. C. Dickey, and C. A. Randall, J. Electroceram. (to be published).
[20]C. Metzmacher and K. Albertsen, J. Am. Ceram. Soc. **84**, 821 (2001).
[21]M. Shiojiri, T. Isshiki, H. Saijo, *et al.*, Phys. Status Solidi A **129**, 353 (1992).
[22]G. Y. Yang, E. C. Dickey, and C. A. Randall, (unpublished).
[23]G. Y. Yang, E. C. Dickey, C. A. Randall, M. S. Randall, and L. A. Mann, J. Appl. Phys. **94**, 5990 (2003).
[24]D. I. Woodward, I. M. Reaney, G. Y. Yang, E. C. Dickey, and C. A. Randall, Appl. Phys. Lett. **84**, 4650 (2004).
[25]S. H. Yoon and H. Kim, J. Mater. Res. **16**, 1479 (2001).
[26]Y. Tsur, T. D. Dunbar, and C. A. Randall, J. Electroceram. **7**, 25 (2001).
[27]C. A. Randall and Y. Tsur, in *Fundamental Physics of Ferroelectronics 2000*, edited by R. E. Cohen (American Institute of Physics, New York, 2000), pp. 238–278.
[28]H. Chazono, T. Hagiwara, and H. Kishi, in *Proceedings of the 11th US-Japan Seminar on Dielectric & Piezoelectric Ceramics*, Sapporo, Japan, 2003, edited by T. Tsurmi and S. Trolier-McKinstry, pp. 1–5.
[29]V. J. Keast, A. J. Scott, R. Brydson, D. B. Williams, and J. Bruley, J. Microsc. **203**, 135 (2001).
[30]R. Brydson, H. Sauer, W. Engel, J. M. Thomas, E. Zeitler, N. Kosugi, and H. Kuroda, J. Phys.: Condens. Matter **1**, 797 (1989).
[31]R. F. Klie and N. D. Browning, Appl. Phys. Lett. **77**, 3737 (2000).
[32]Hans Lüth, *Surfaces and Interfaces of Solids*, 2nd ed. (Springer, Berlin, 1993).
[33]S. D. Berger, J. M. Macaulay, and L. M. Brown, Philos. Mag. Lett. **56**, 179 (1987).
[34]M. Sankaraman and D. Perry, J. Mater. Sci. **27**, 2731 (1992).
[35]R. D. Leapman, L. A. Grunes, and P. L. Fejes, Phys. Rev. B **26**, 614 (1982).
[36]R. D. Leapman and L. A. Grunes, Phys. Rev. Lett. **45**, 397 (1980).
[37]M. T. Otten, B. Miner, J. H. Rask, and P. R. Buseck, Ultramicroscopy **18**, 285 (1985).
[38]R. Brydson, H. Sauer, and W. Engel, in *Transmission Electron Energy Loss Spectroscopy in Materials Science*, edited by M. M. Disko, C. C. Ahn, and B. Fultz (Warrendale, Pennsylvania, 1991), pp. 131–154.
[39]D. P. Cann and C. A. Randall, J. Mater. Res. **12**, 1685 (1997).